Proceedings of the ASME 2018 International Design Engineering Technical Conferences & Computers and Information in Engineering Conference
IDETC/CIE 2018
August 26-29, 2018, Quebec City, Canada

DETC2018/MR-85371

A 3D-PRINTED NEEDLE DRIVER BASED ON AUXETIC STRUCTURE AND INCHWORM KINEMATICS (AUTHOR MANUSCRIPT, PUBLISHER VERSION DOI 10.1115/DETC2018-85371)

A. Pfeil, L. Barbé, B. Wach, A. Bruyas, F. Geiskopf, M. Nierenberger and P. Renaud
ICube, INSA Strasbourg - CNRS - University of Strasbourg, France
Email: a.pfeil@unistra.fr

ABSTRACT

Linear actuation is a basic need in robotized manipulation of surgical instruments, that must comply with a challenging environment in terms of safety, compactness and now often compatibility with imaging modalities like CT or MRI. In this paper, we focus on needle manipulation for interventional radiology. We propose a needle driver, i.e. a linear actuator for needle insertion, based on the inchworm principle combined with pneumatic energy. Our first contribution is to propose, model and implement the device using a so-called auxetic structure. Its use increases achievable displacement under pressure and provides sufficient off-axis stiffness to use the actuator without additional guidance. Simplified modeling is introduced for the actuator synthesis. Our second contribution is to implement the actuator with multimaterial additive manufacturing combining rigid and flexible materials to increase compactness. As a third contribution, initial assessment of component sterilization and compatibility with X-ray and MRI imaging modalities is presented.

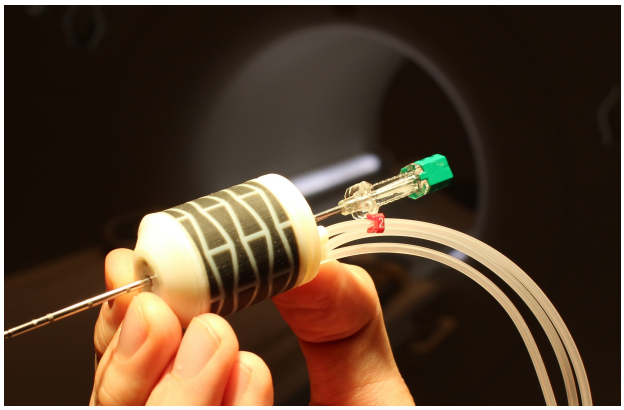

FIGURE 1: PROTOTYPE OF THE NEEDLE DRIVER.

1 INTRODUCTION AND RELATED WORK

Linear actuation is a basic need in robotized manipulation of surgical instruments. In minimally invasive surgery, motorized translation is being used for surgical instruments and endoscope [1]. The design of actuators is then challenging since it must comply with the operating room environment in terms of safety, compactness, asepsy. In hybrid surgery and interventional radiology (IR), compatibility with imaging devices such as CT or MRI scanners is now also often mandatory. Several designs have been introduced in particular in the context of IR to perform remotely needle insertion in percutaneous procedures, using rotary actuation and friction-based transmision [2,3], pneumatic [4,5] or electric actuation [6] with graspers to insert a needle step by step, providing unlimited range of motion. Pneumatic actuation offers then compatibility with imaging devices. Step by step motion is also adopted with inchworm kinematics [7] as implemented in [8] using piezoelectric actuation. Inchworm kinematics are of particular interest for the compactness they can provide. Their use in conjunction with pneumatic energy was proposed in [9] using additive manufacturing for implementation. Safety with inchworm kinematics was then highlighted, as the maximum displacement by step can be adjusted by design.

Additive manufacturing is indeed of interest for the freedom of shape in part design. In addition, new design solutions for robotics can be introduced when considering now available custom [10] or commercial [11–13] multimaterial additive manufacturing (MMAM) techniques, such as compliant joints [14] or brake and sensing solutions [15]. Considering MMAM for actuator design, it is then in particular possible to consider meta-materials that offer non conventional behavior as described in [16] and yet scarcely exploited in robot design [17]. Our proposition is therefore to use MMAM to develop a linear actuator based on the inchworm principle with pneumatic energy, shown in Fig. 1. In particular, we describe here the introduction of an auxetic structure [16] to increase actuator kinematic performance and ensure its stiffness properties, so it can be used to create motion and perform guidance at the same time. By keeping off-axis stiffness satisfactory, no additional prismatic joint is thus needed. In the following, the actuator development is presented for IR with the introduction of a needle driver. The provided design can however be adapted to other surgical instruments as well.

In section 2, the driver principle, its design and simplified model for synthesis are introduced. In section 3, implementation and initial characterization is presented to evaluate the actuator performances. Section 4 is dedicated to design evolution, with special attention to the possibility of performing sterilization and avoid needle contamination during insertion. Finally, conclusions on the new actuator and further applications in medical context are discussed in section 5.

2 ACTUATOR PRINCIPLE AND DESIGN

2.1 Specifications for a needle insertion actuator

Biopsy for diagnosis is one of the most frequent tasks in IR. Needle insertion in liver or kidney is then characterized by maximum insertion forces around 2 N [18]. It has to be performed in about 2 minutes for a 60-mm insertion according to radiologist feedback. Such a duration is long enough to monitor safely the progression, and it means the desired needle average velocity is about 0.5 mm/s.

Stiffness in directions perpendicular to the needle, designated in the following as off-axis stiffness, is of importance to maintain accuracy. Since we want to use the actuator without additional guiding element, its stiffness needs to be significantly higher than the needle one. We set the actuator stiffness to be at least 6 times the needle stiffness. Biopsy is usually performed with a 19G needle (diameter of 1.07 mm), made out of stainless steel (Young's modulus of 200 GPa). This means the off-axis stiffness of the actuator must be greater or equal to 14.8 N/mm.

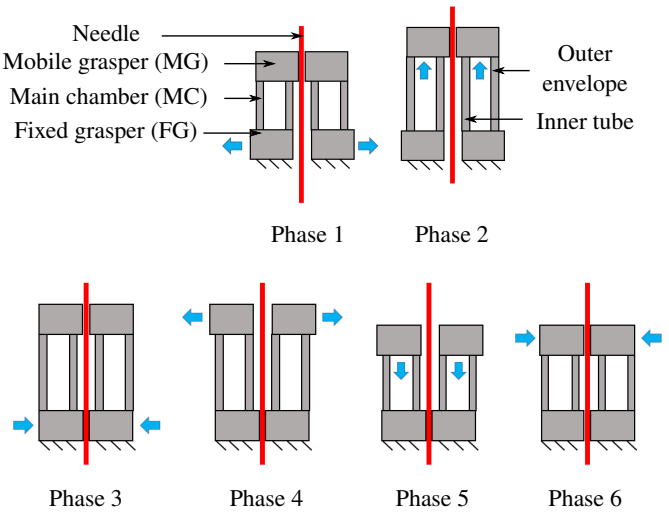

FIGURE 2: DIFFERENT PHASES OF MOTION FOR THE INCHWORM CYCLE.

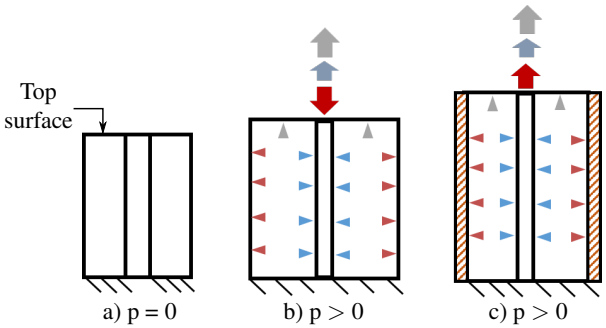

FIGURE 3: SECTION VIEW OF THE MAIN CHAMBER: a) WITHOUT PRESSURE; b) WITH PRESSURE, CONVENTIONAL OUTER ENVELOPE; c) WITH PRESSURE, AUXETIC-BASED OUTER ENVELOPE.

2.2 Overall structure and control

Three elements are needed to implement inchworm kinematics: two graspers and one main chamber, that generates a translation between the two graspers, as depicted in Fig. 2. Since the actuator has to guide properly the needle, a symmetry of revolution of the actuator about the needle axis appears naturally of interest to control the off-axis stiffness. This means the main chamber (Fig. 2) is of annular shape, defined by two planar surfaces perpendicular to the needle and two cylindrical surfaces, one that defines the outer envelope of the actuator and the other one that creates what we designate as the inner tube around the needle. The sequence for motion generation is presented in Fig. 2: the needle is advanced by successive grasping/releasing of the needle and inflation of the main chamber. Blue arrows indicate the actions performed during each phase of the sequence. Actuator

dynamics and thus needle insertion velocity are then linked to the behavior of the main chamber and the graspers.

During inflation (Phase 2), the inner surfaces of the main chamber are submitted to pressure to create motion as represented on Fig. 3. On that figure, a single color is used to model the pressure applied on one surface (triangle symbols) and the corresponding induced axial displacement (arrow sign) of the chamber top surface. If we analyze independently the contribution of the different surfaces, we can see that the pressure on the top surface (in grey) generates an axial elongation of the chamber. Similarly, pressure on the inner tube (in blue) tends to create an elongation due to Poisson effect. On the contrary, the radial pressure on the outer envelope creates a radial expansion, if conventional materials are used. This radial expansion induces an axial contraction of the chamber, as shown in Fig. 3b). Contradictory motions are thus generated, which is not in favor of the actuator efficiency. With an auxetic material [16], a reverse effect can be obtained thanks to its negative Poisson's ratio. This means we propose to create the outer envelope using an auxetic pattern, so that this surface also contributes to the axial displacement instead of creating axial compression, as shown in Fig. 3 c), the auxetic outer envelope being represented by the red hatched surface.

2.3 Design of graspers and outer envelope

2.3.1 MMAM specifications The Polyjet technology (Stratasys Ltd, USA) allows the production of monolithic parts composed of several materials. It was successfully considered in previous works for the design of compliant joints [14], and robotic structures [15, 19]. We therefore select this MMAM process for implementation in the following and use Verowhite and TangoBlack Plus materials, following their commercial denominations. Their mechanical properties have been characterized previously, as presented in [14]. The first material is an elastic material, with Young's modulus equal to 2000 MPa and yield stress equal to 25 MPa. The other material has properties similar to elastomers, with a quasi-incompressible behavior in compression. It will thus be designated as a rubber-like material. When small deformations are applied to this material, a linear approximated model can be used with Young's modulus of 0.8 MPa.

The Polyjet process is based on photopolymerization. In addition to the two previous materials, a support material is being used during production. This impacts the design of the actuator when hollow cavities need to be created. Using a Connex 350 system, thickness of material layers is equal to 30 microns, and in-plane resolution to 42 microns. Internal experiments show the manufacturing accuracy is between 10 and 100 microns in standard conditions, with a minimal size of geometrical features equal to 1 mm.

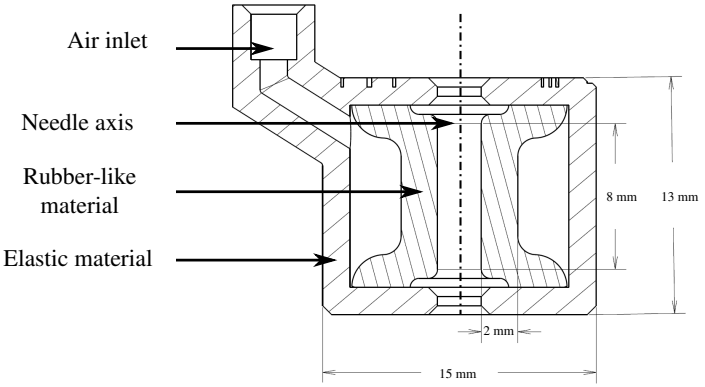

FIGURE 4: SECTION VIEW OF THE GRASPER.

2.3.2 Grasper design. Grasper design is constrained by the needle size and the required forces for needle insertion and extraction. Its dynamics also affect the needle motion as mentioned in section 2.2. Grasping by friction is thus preferred compared to solutions based on linkages as described in [6]. With pneumatic actuation, the dynamics are influenced by the volume of compressed air. The volume of the chamber created around the needle is therefore minimized as presented in the design of Fig. 4. Dimensions are here constrained by the size of minimum geometrical features that can be obtained with the MMAM process. The rubber-like material is selected for the inner surface of the grasper: its low stiffness helps to minimize the pressure level needed to grasp the needle, and it provides friction with the needle comparable to silicone.

The geometrical profile of the inner surface is composed of a linear section for contact with the needle, and two curved sections at the ends to ease the surface deformation during grasping. The thickness of the flexible part is set to 2 mm and the length of the linear section is set to 8 mm, values determined using initial development for MR elastography [20].

2.3.3 Outer envelope design This envelope is designed to close the main chamber with use of the auxetic effect. Several patterns have been proposed to get this effect [21, 22]. We here focus on the inverted honeycomb pattern. It is indeed simple to build a cylindrical shape using the unit cell represented in Fig. 5 a). The cell can be circularly repeated to create a ring, and then several rings connected to obtain the cylindrical auxetic structure depicted in Fig. 5 b). Thanks to the configuration of the struts, once the unit cells are placed in a circular configuration in the actuator structure, an expansion of the circumference of the tube involves its elongation along its axis. In addition, the truss that is created in this way is in favor of the off-axis stiffness, thanks to the continuity of the structure.

For implementation, the auxetic structure is realized with the

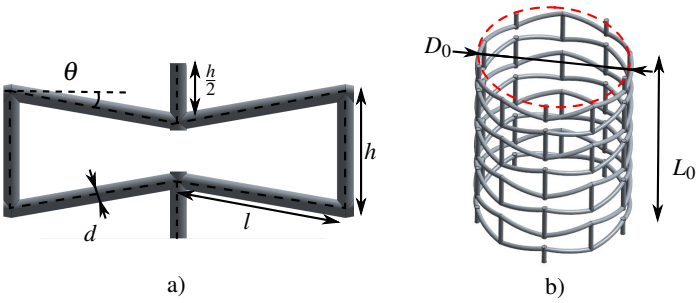

FIGURE 5: DESIGN OF THE AUXETIC STRUCTURE: a) UNIT CELL, b) OVERALL STRUCTURE.

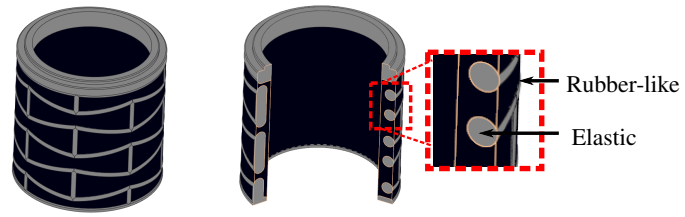

FIGURE 6: GLOBAL a) AND CUTAWAY b) VIEWS OF THE OUTER ENVELOPE.

elastic material, while a rubber-like material is added between the struts of the auxetic structure to seal the envelope for pressurization, as represented in Fig. 6 b), with a cutaway view of the actuator. The outer envelope (Fig. 6 a)) can be produced in one part taking advantage of the considered MMAM process.

2.4 Modeling of the outer envelope

For synthesis, it is needed to establish relationship between the actuator geometry and the desired performances, in terms of force, velocity that is linked to the displacement provided by the main chamber, and the off-axis stiffness. A simplified modeling is therefore developed, using a quasi-static analysis.

2.4.1 Parameterization. The inverted honeycomb unit cell is defined (Fig. 5) by l, θ, respectively the length and inclination of slanted struts, h the length of vertical struts, d the diameter of struts. The structure is built by repetition of the unit cell with N_c and N_v circumferential and axial repetitions to create a structure of length L_0 and diameter D_0. Because of the inverted honeycomb shape and the way the unit cells are assembled, two relationships exist between the parameters, so that the structure is described by six independent parameters:

$$h = \frac{L_0}{2.N_v} + l.sin(\theta) \tag{1}$$

$$l = \frac{\pi.D_0}{2.N_c.cos(\theta)} \tag{2}$$

2.4.2 Behavior of the auxetic structure. In [21], the structural stability of a similar structure under compression has been studied. It was shown that it is possible to describe the structure behavior by considering this latter as a continuous tube made of an homogeneous orthotropic material. Its properties are directly linked to the unit cell geometry and the number of cells in the tube, with four coefficients to describe the behavior of the equivalent tube when submitted to the internal pressure [21]:

1. the Young's modulus in the axial direction E_z
2. the Young's modulus in the circumferential direction E_c
3. the Poisson's coefficient $\nu_{cz} = -\frac{\varepsilon_z}{\varepsilon_c}$, the ratio between tube axial and circumferential strains when submitted to an an axial load
4. the shear modulus G_{cz} describing the ratio between the shear stress in the tube wall and the corresponding shear strain.

We consider small deformations for the material of the structure. In addition, the inverted honeycomb shape provides an auxetic effect only if the slanted struts have a slender shape ($d \ll D_0$) and if their flexion is the main source of deformation [23,24]. In such a situation, the four coefficients can be expressed as below with E the Young's modulus of the elastic material used for the auxetic structure:

$$\nu_{cz} = -\frac{\cos\theta}{\left(\frac{h}{l} - \sin\theta\right).\tan\theta} \tag{3}$$

$$E_z = \frac{3.E.\left(\frac{h}{l} - \sin\theta\right)}{2.\pi^2}.\left(\frac{d.N_c}{D_0}\right)^3 \tag{4}$$

$$E_c = \frac{3.E.\cos^2\theta}{2.\pi^2.\left(\frac{h}{l} - \sin\theta\right).\tan^2\theta}.\left(\frac{d.N_c}{D_0}\right)^3 = \nu_{cz}^2 E_z \tag{5}$$

$$G_{cz} = \frac{3.E.\left(\frac{h}{l} - \sin\theta\right).\cos^2\theta}{2.\pi^2.\left(\frac{h}{l}\right)^2.\left(1 + \frac{2.h}{l}\right)}.\left(\frac{d.N_c}{D_0}\right)^3 \tag{6}$$

2.4.3 Derivation of envelope elongation. The envelope elongation under application of the pressure P in the main chamber, with the force F generated by the actuator at its end, is obtained using the virtual work principle as used for McKibben actuators [25–27]. We therefore consider the static equilibrium of the actuator, and the balance of input and output works respectively denoted as dW_{in} and dW_{out}. The input work can be decomposed between radial and axial elongations [25], with (r, L) re-

spectively the structure radius and length and (dr, dL) their variations:

$$\begin{aligned} dW_{in} &= (2.\pi.P.L.r).dr + (\pi.r^2.P).dL \\ &= P.dL.(2.\pi.L.r.\frac{dr}{dL} + \pi.r^2) \end{aligned} \tag{7}$$

From the definition of ν_{cz}, one can derive with $\varepsilon_z = dL/L_0$ the axial strain and $\varepsilon_c = dr/r_0$ the circumferential strain:

$$\begin{aligned} \frac{dr}{dL} &= -\frac{r_0}{L_0}.\frac{1}{\nu_{cz}} \\ r &= r_0(1 - \frac{\varepsilon_z}{\nu_{cz}}) \end{aligned} \tag{8}$$

so that after simplifications, the input work is equal to:

$$dW_{in} = P.\frac{\pi r_0^2 L_0}{\nu_{cz}^2}.\varepsilon_z.\left[3\varepsilon_z^2 + (2 - 4\nu_{cz})\varepsilon_z + (\nu_{cz}^2 - 2\nu_{cz})\right] \tag{9}$$

The output work is the sum of radial and axial works following [25]:

$$dW_{out} = -F_a.dL - F_r.dD \tag{10}$$

with F_r and F_a the resulting radial and axial forces. The axial resulting force is the sum of the force F and the elastic force due to the stiffness of the inner tube and outer envelope. The inner tube is designed to fit around the needle. This means it is of small section compared to the auxetic structure, and we assume its stiffness can be neglected during the actuator synthesis. Given the Young's modulus of elastic and rubber-like materials, we also consider the axial stiffness denoted K_z is only due to the auxetic structure in the outer envelope and do not model the influence of the rubber-like material in this latter. Then one has:

$$F_a = F + K_z.dL = F + \frac{S_t.E_z}{L_0}.dL \tag{11}$$

with S_t the surface in a plane perpendicular to its axis of the continuous tube made of homogeneous material with properties defined in section 2.3.2: $S_t = \frac{\pi}{4}.\left((D_0 + d)^2 - (D_0 - d)^2\right)$. Similarly, the radial resulting force F_r is due to the radial stiffness of the auxetic structure and is equal to:

$$F_r = \left(\frac{2.E_c.d.L_0}{D_0}\right)\left(\frac{-D_0.\varepsilon_z}{\nu_{cz}}\right) \tag{12}$$

Expressing the balance between input and output work we finally obtain

$$3.\varepsilon_z^2 + B(P).\varepsilon_z + C(F,P) = 0 \tag{13}$$

with

$$\begin{aligned} B(P) &= 2 - 4.\nu_{cz} - \frac{\pi+2}{\pi/2}.\frac{2.d}{D_0}.\frac{E_c}{P} \\ C(F,P) &= \nu_{cz}^2 - 2.\nu_{cz} - \frac{4.\nu_{cz}^2 F}{\pi.D_0^2.P} \end{aligned} \tag{14}$$

The discriminant $D(P,F)$ of the quadratic equation is

$$D(P,F) = B(P)^2.\left(1 - \frac{12.C(F,P)}{B(P)^2}\right) \tag{15}$$

The term $B(P)$ is a function of E_c/P. The Young's modulus E_c is typically in the order of several hundreds of MPa, whereas internal pressure is a few bars, i.e. less than 1 MPa. The absolute value of $B(P)$ is therefore governed by the third term in Eqn. (14), which is very large compared to the terms in $C(F,P)$, and a first-order approximation of $D(P,F)$ can be used to express ε_z:

$$\varepsilon_z = -\frac{C(F,P)}{B(P)} = \frac{\left(\nu_{cz}^2 - 2.\nu_{cz} - \frac{4.\nu_{cz}^2 F}{\pi.D_0^2.P}\right)}{\left(\frac{\pi+2}{\pi/2}.\frac{2.d}{D_0}.\frac{E_c}{P}. + 4\nu_{cz} - 2\right)} \tag{16}$$

This relationship allows us first to see the impact of the auxetic effect. Indeed, if the value of ν_{cz} is becoming negative, as it is the case for an auxetic structure, the numerator and denominator in Eqn. (16) are respectively increasing and decreasing. As a result, the value of the reachable axial strain ε_z is being increased. For a given length, using an auxetic structure allows us to increase the motion generated by pressure application. Second, it is now possible to predict the actuation elongation as $\Delta L = \varepsilon_z.L_0$.

2.4.4 Off-axis stiffness.

Thanks to the introduction of an homogeneous equivalent material in section 2.4.2, simple beam theory results can be employed to obtain the lateral actuator stiffness in the actuator initial configuration. Its expression is reported in Eqn. (17) with $I = \pi/64((D_0 + d)^4 - (D_0 - d)^4)$ the second moment of inertia of the cylindrical homogeneous element equivalent to the auxetic structure.

$$K_x = \frac{3.E_z.I}{L_0^3} \tag{17}$$

2.5 Determination of actuator geometry

Using Eqn. (16) and Eqn. (17) it is now possible to perform the synthesis of the actuator. Three limits need to be taken into account. First, geometrical constraints exist on the geometry of the auxetic structure. The structure is feasible only if the value of θ belong to $]0, \theta_{max}]$ in degrees, with θ_{max} being defined in Eqn. (18).

$$\theta_{max} = \frac{180}{\pi}.\arcsin\left(\frac{h-d}{2.l}\right) \tag{18}$$

Second, the elastic material has a limited stress domain. Maximum stress σ_{max} is encountered in the slanted struts of the auxetic cells, submitted to bending with an overall displacement of the structure that equals $\varepsilon_z L_0$. Using results from beam theory, it is then possible to obtain the condition in Eqn. (19).

$$\sigma_{max} = \frac{3.E.d.L_0.\varepsilon_z}{2.N_v.l^2} \tag{19}$$

Finally, limitations are related to the manufacturing process, as described in section 2.3.1.

Synthesis is performed by considering first the application constraints. The outer diameter of the actuator is chosen to keep it compact and compatible with an integration in a robotic device such as the one presented in [15]: $D_0 = 27$ mm and $L_0 = 25$ mm. The pressure is chosen equal to 1 bar, a low value for safety. The selection of the geometry is performed by computing the elongation ΔL / stiffness K_x domain for designs obtained after discretization of parameters: $N_c \in [4,8]$, step: 1; $N_v \in [2,5]$, step: 0.5; $\theta \in [5,45]$, step: 1°; $d \in [1,3]$, step: 0.1 mm. For each combination of geometrical parameters, the model is applied in order to compute the value of ΔL. It is then verified that $\theta < \theta_{max}$, $\sigma_{max} < 25$ MPa, and that the stiffness K_x is at least 6 times the needle stiffness in order to guide properly this latter. All the geometries that respect the three constraints are compared and the geometry that presents the most important value of ΔL is chosen. Final geometry is defined by $(D_0, L_0, N_c, N_v, \theta, d) = (27\,\text{mm}, 25\,\text{mm}, 4, 2.5, 10°, 2.2\,\text{mm})$, which allows to generate 1.1 mm of displacement under 2 N, and it provides a stiffness K_x = 16.1 N/mm.

3 Implementation and initial characterization

3.1 Integration and manufacturing

The graspers and outer envelope are integrated as represented in Fig. 7. The three air inlets are integrated on the same side, to avoid pneumatic tubes arriving close to the tissues. The three chambers are materialized in color on the figure: in green the fixed grasper (FG) chamber, in red the chamber of the mobile grasper (MG) and in blue the main chamber (MC). Inner tube dimensions are chosen to maximize the surface supporting axial pressure, beneficial to the axial displacement. Rings of elastic material are added to the inner tube to avoid any contact between the inner tube and the needle during pressurization.

Since the support material for printing needs to be removed, the actuator cannot be printed all-at-once. It is composed of five parts shown in Fig. 8: the fixed grasper (1), the upper flange (2), the outer envelope (3) the inner tube and mobile grasper (4), and the cap (5). The support material is removed mechanically with tools and then with pressurized water. To ease the removal of support material in the inner chambers of the graspers,

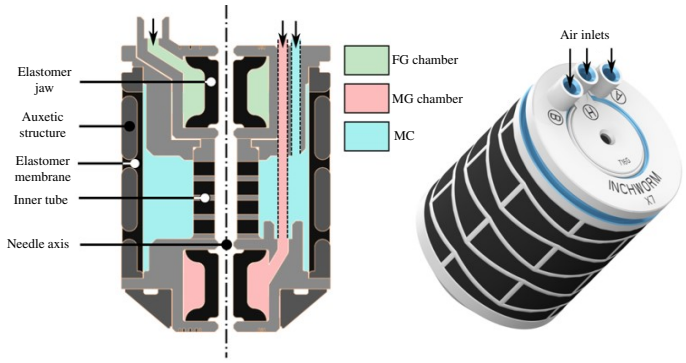

FIGURE 7: CAD DESIGN OF THE ACTUATOR: a) CROSS SECTIONAL VIEW, b) FULL VIEW.

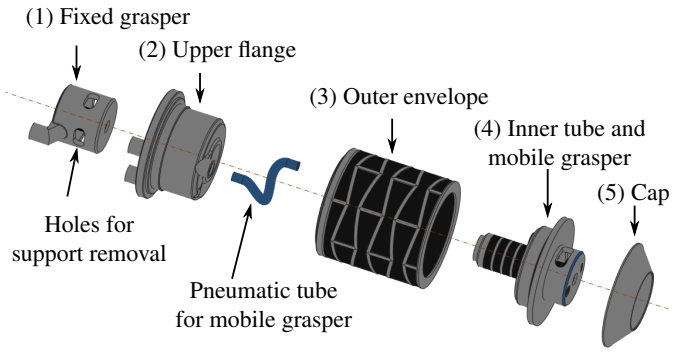

FIGURE 8: EXPLODED VIEW OF THE ACTUATOR.

holes have been added on the periphery of their outer cylindrical walls, as shown Fig. 8. The components are glued together using cyanoacrylate adhesive. The actuator overall length is equal to 40 mm, with external diameter of 29.2 mm (Fig. 1).

3.2 Control

The scheme of the pneumatic circuit is represented in Fig. 9. It is composed of a pump and a reservoir, two servo-valves (VPPM-6L, Festo AG), three fast switching valves (MHE2-MS1H-3/2G, Festo AG) and three pressure sensors (SPTWP6R, Festo AG). The servo-valves are used for pressure regulation. Pressure is set to 3 bars for fixed (FG) and mobile (MG) graspers while a pressure of 1 bar is used for the main chamber (MC). Time evolution of pressure is controlled using control signals CV1, CV2 and CV3. The pressure measurements are not mandatory for the control and are here used for monitoring. Control software is run on a PC with RT Linux Xenomai kernel.

3.3 Characterization

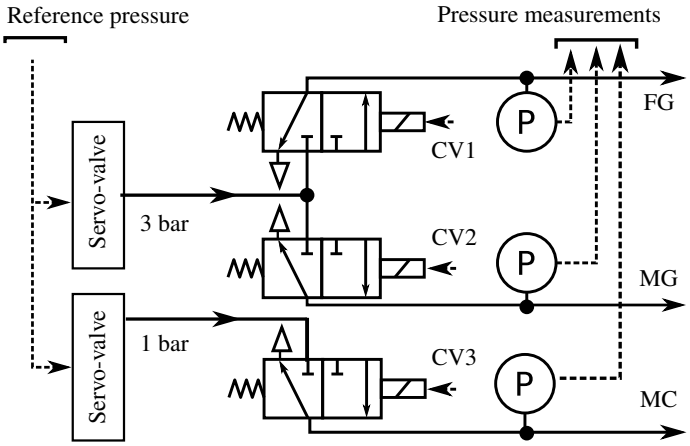

FIGURE 9: SCHEME OF ACTUATOR PNEUMATIC CIRCUIT.

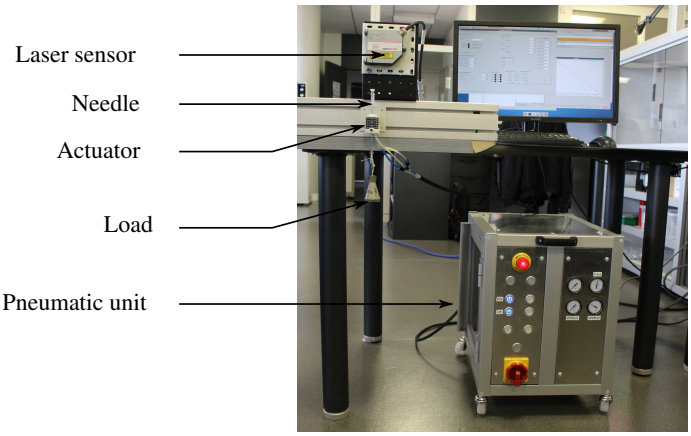

FIGURE 10: SETUP FOR EXPERIMENTAL DISPLACEMENT/FORCE EVALUATION

3.3.1 Protocol and experimental setup. The setup visible on Fig. 10 is used to evaluate the displacement/force characteristics. The actuator is positioned vertically. The displacement of the needle tip is measured with a laser-based contactless sensor (Opto NCDT 2300, MicroEpsilon, 0.8 μm resolution). A flat target surface is fixed on the tip of the needle to ease the laser-based measurement. Loading is performed by attaching weights to the bottom part of the needle. First, only the displacement provided by the main chamber is measured when the needle is grasped without and with a 2 N load. Second, the needle motion is recorded when the actuator control sequence of Fig. 2 is applied, again without and with a 2 N load. Third, the off-axis stiffness of the actuator is determined by placing the actuator in an horizontal configuration, so that loading is performed using different weights suspended at the free end of the actuator. Corresponding displacements are then measured by vision (Canon EOS 700D camera, 18 MPixel resolution) and stiffness is determined as the slope of the force-deflection characteristic.

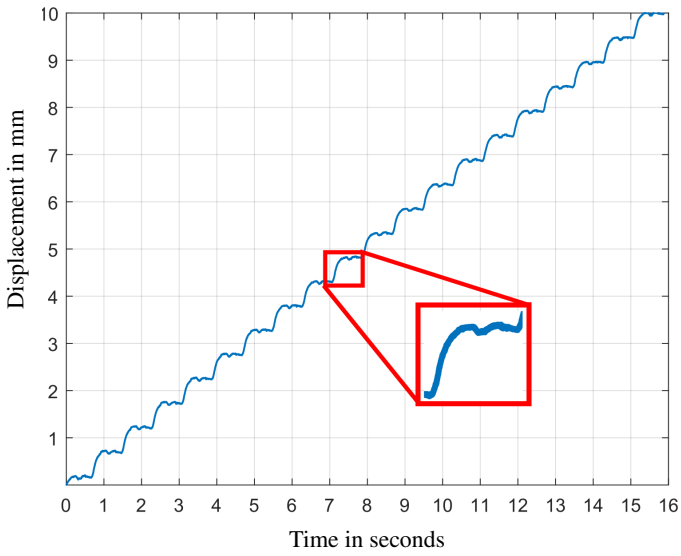

FIGURE 11: MEASUREMENT OF ACTUATOR NO-LOAD DISPLACEMENT.

3.3.2 Results and discussion. Prior to evaluation, the control sequence was adjusted experimentally: minimal time for grasper pressurization is identified to be equal to 80 ms to ensure a correct needle grasping and the inchworm cycle is set to 1.2 Hz. This means according to Fig. 2 that the pressurization in the main chamber lasts 250 ms.

Experiments show that pressurization of the main chamber generates a displacement of 0.92 mm after 4 seconds. This value is close to the value of 1.1 mm computed with the simplified modeling. The influence of the rubber-like material in the outer envelope and in the inner tube is probably here observed. In 250 ms, reachable displacement is equal to 0.56 mm, which can indicate an influence of viscoelastic behavior of the materials. Application of the load does not produce measurable difference on the displacement of the main chamber.

Needle displacement with the inchworm sequence leads to a no-load velocity of 0.64 mm/s, with displacement profile represented on Fig. 11. Velocity with a 2N-load lowers to reach 0.34 mm/s. As the load does not affect the main chamber displacement, as mentioned above, the velocity reduction may be explained by the flexibility of the graspers. The reduction of actuator velocity is however observed here in a worst-case scenario, since the load is constant during the whole inchworm cycle. In the applicative context, resistive forces of tissues are indeed mostly applied during needle advance steps, corresponding to Phase 2 on Fig. 2. In any case, with the proposed implemented

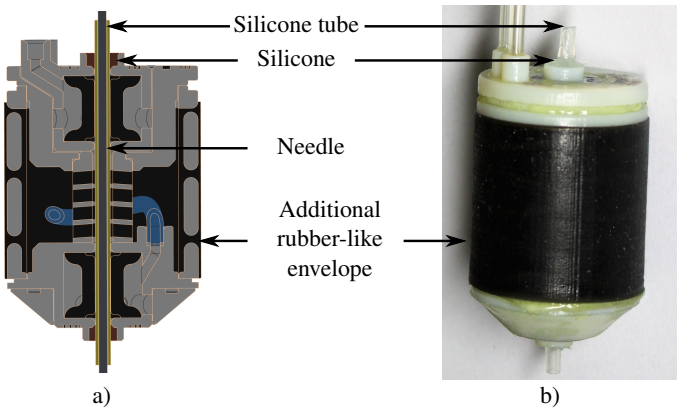

FIGURE 12: IMPROVED DESIGN: (a) CAD SECTION VIEW; (b) ACTUATOR AFTER STERILIZATION.

solution, a velocity of 0.34 mm/s, close to the targeted value, can still be achieved with the selected severe conditions.

Finally, evaluation of flexural stiffness yields an off-axis stiffness of 8 N/mm, which is 3 times the needle stiffness, but only half of the value computed with the auxetic structure modeling. We probably observe the contribution of other parts used in the assembly depicted in Fig. 8.

Experimental characterization shows that after some time, fatigue cracks tend to appear on the outer surface, with the subsequent appearance of leakage in the main chamber. The lifetime of this initial design is thus not optimal. At this stage, sterilization is also not yet validated, and the contact between 3D printed material and the needle can cause biocompatibility issues. These three aspects are thus investigated in a second step.

4 DESIGN IMPROVEMENT

4.1 Improvement of actuator endurance

In order to improve the component lifetime, a 0.5-mm thick envelope of rubber-like material is added on the outside of the actuator. In addition, the design of the inner tube is modified with a 4° tilting of the interfaces between the two materials to suppress risks of tearing at the junctions. A section view of the improved actuator is shown in Fig. 12 a).

Endurance of the modified component is assessed using the previous experimental setup. The actuator lifts a needle submitted to a 2-N load to reach a cumulated needle displacement of 600 mm, with continuous recording of needle position. After such overall needle displacement, no significant variation of actuator behavior is observed. This means satisfactorily that the actuator can at the moment be used either as a single-use component or for repetitive use for at least 10 typical insertions of 60 mm.

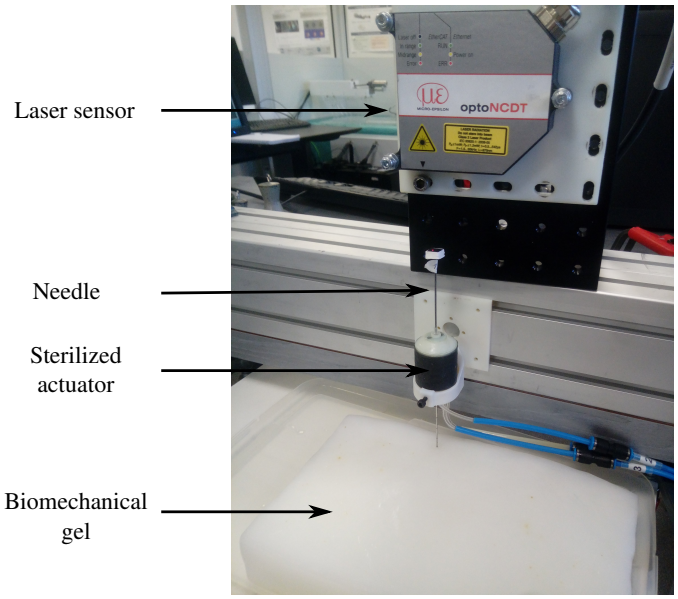

FIGURE 13: INSERTION IN A BIOMECHANICAL GEL.

4.2 Design update for medical use

The materials being used are not today certified as biocompatible. To avoid any contamination of the needle, the actuator is modified as shown on Fig. 12 with integration of a silicone tube (inner diameter 1.5 mm, outer diameter 2.3 mm, Deutsch & Neumann GmbH, Germany). At both ends of the actuator, a short annular shape is also added, to help gluing the tube with silicone to the rigid material.

Few information can be found concerning the sterilization of the VeroWhite and TangoBlack Plus materials in the literature. Sterilization by gamma irradiation was successfully implemented for VeroWhite parts [28], with doses between 25 and 35 kGy. This method is therefore chosen and sterilization is performed on specimens for material testing and on the whole needle driver.

Standard tensile tests (ISO 527-1) on both materials are performed before and after sterilization of samples for characterization purpose. After a radiation dose of 34 kGy, Young's modulus of elastic material is increased from 1830 MPa to 2810 MPa. Conversely, no significant difference is observed for the rubber-like material. As an initial assessment, the component after sterilization is also characterized using the previous protocol. First, it is observed that the whole component is functional after sterilization. Second, the no-load velocity is not significantly affected by the sterilization. This needs to be more investigated, in particular at the level of the main chamber behavior, as the material stiffness increase could impact the component behavior.

To be closer to the applicative context, additional evaluation is performed by achieving needle insertion in a biomechanical phantom, preferred to a constant load given the previous remark

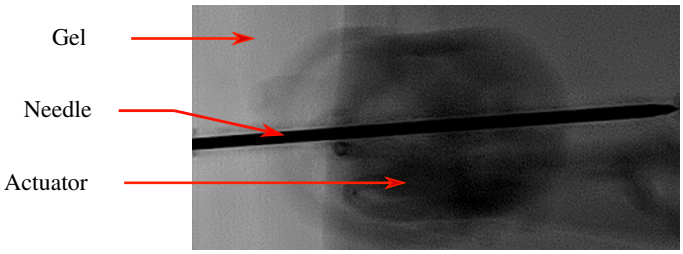

FIGURE 14: X-RAY IMAGE OF ACTUATOR WITH NEEDLE POSITIONED ON A GEL.

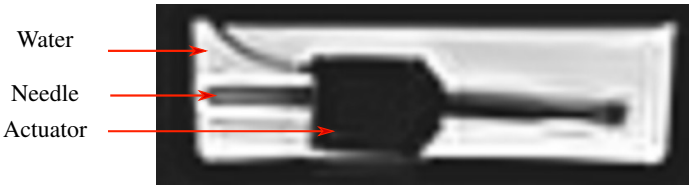

FIGURE 15: MRI IMAGE OF ACTUATOR WITH NEEDLE IMMERSED IN WATER.

on force variation in tissues. A 5% PVA gel phantom reproducing properties of liver tissue [29] is being used. The experimental setup is shown on Fig. 13. The sterilized actuator is able to insert a needle at a speed of 0.4 mm/s, which is similar to the speed without sterilization, and acceptable for the considered procedure.

Finally, compatibility with imaging devices is being evaluated. Figure 14 represents an X-ray image of the actuator with needle placed in the phantom, acquired with a Cone Beam CT system (Allura FD20, Philips Healthcare, The Netherlands). Figure 15 represents the actuator with a MR-compatible needle immersed in water as observed in a MRI scanner (BLADE sequence, MAGNETOM Aera 1.5 T, Siemens Healthineers, Germany). In the first case, the actuator does not create any artifact in the images and can be considered radio-transparent compared to the needle. In the second case, the actuator causes no deformation either: the diameter of the actuator as computed from the images is equal to its real value, whereas the needle size appears in the image four times its real value.

5 CONCLUSION

In this paper, a new pneumatic needle driver is introduced, that is based on an auxetic structure and the inchworm principle. Its analytical modeling, synthesis, experimental characterization have been introduced as well as its implementation with MMAM. Combination of MMAM, inchworm kinematics and pneumatic energy leads to a compact component, able to move and guide a needle in IR. The auxetic-based design is interesting for improving the use of pressure inside the component to generate the motion. This was outlined qualitatively and from the provided auxetic structure model. The performances observed experimentally are relevant for the medical task in terms of velocity and stiffness for guidance. In addition, the usability of the component in the medical context was investigated, with demonstration of needle insertion in biomechanical phantom of a sterilized version which endurance is also promising.

Experimental characterization outlines two interesting developments to conduct. First, the prediction accuracy of the actuator model could probably be improved by considering the contribution of rubber-like material. Second, the grasper design should be improved since it impacts the motion characteristics. The variation of velocity when load on the needle increases is however today not a strong issue, since the control of the needle progression is anyway performed by the radiologist from the medical images.

It will now be interesting to consider the integration of the proposed needle driver in a robotic tool holder for IR. Another axis of development will be to derive other drivers using the same principle for manipulation of surgical tools in the context of minimally invasive surgery.

ACKNOWLEDGMENT

The authors would like to thank Q. Boehler and L. Meylheuc for help in experimental evaluation, M. de Wild and F. Schuler from FHNW and Synergy Health Däniken AG for gamma sterilization. This work was supported by the INTERREG Upper Rhine program from the ERDF (European Regional Development Fund), SPIRITS project, as well as the Investissements d'Avenir (Robotex ANR-10-EQPX-44, Labex CAMI ANR-11-LABX-0004).

REFERENCES

[1] Gumbs, A. A., Crovari, F., Vidal, C., Henri, P., and Gayet, B., 2007. "Modified Robotic Lightweight Endoscope (ViKY) Validation In Vivo in a Porcine Model". *Surgical Innovation,* ***14***(4), Dec., pp. 261–264.

[2] Stoianovici, D., Cleary, K., Patriciu, A., Mazilu, D., Stanimir, A., Craciunoiu, N., Watson, V., and Kavoussi, L., 2003. "Acubot: a robot for radiological interventions". *IEEE Transactions on Robotics and Automation,* ***19***(5), pp. 927–930.

[3] Walsh, C. J., Hanumara, N. C., Slocum, A. H., Shepard, J.-A., and Gupta, R., 2008. "A patient-mounted, telerobotic tool for CT-guided percutaneous interventions". *ASME Journal of Medical Devices,* ***2***(1), pp. 011007–011007–10.

[4] Muntener, M., Patriciu, A., Petrisor, D., Schar, M., Ursu, D., Song, D., and Stoianovici, D. Y., 2008. "Transperineal prostate intervention: Robot for fully automated MR imag-

ing system description and proof of principle in a canine model". *Journal of Radiology,* ***247***(2), pp. 543–549.

[5] Bricault, I., Zemiti, N., Jouniaux, E., Fouard, C., Taillant, E., Dorandeu, F., and Cinquin, P., 2008. "Light puncture robot for CT and MRI interventions". *IEEE Engineering in Medicine and Biology Magazine,* ***27***(3), pp. 42–50.

[6] Piccin, O., Renaud, P., Barbé, L., Bayle, B., Maurin, B., and de Mathelin, M., 2005. "A Robotized Needle Insertion Device for Percutaneous Procedures". In Proceedings of ASME International Design Engineering Technical Conferences, Vol. 7, pp. 443–440.

[7] May, J. W. G., 1975. Piezoelectric electromechanical translation apparatus, Aug. 26. US Patent 3,902,084.

[8] El Bannan, K., Chronik, B. A., and Salisbury, S. P., 2015. "Development of an MRI-compatible, compact, rotary-linear piezoworm actuator". *ASME Journal of Medical Devices,* ***9***(1), pp. 014501–014501–7.

[9] Comber, D. B., Slightam, J. E., Gervasi, V. R., Neimat, J. S., and Barth, E. J., 2016. "Design, additive manufacture, and control of a pneumatic MR-compatible needle driver". *IEEE Transactions on Robotics,* ***32***(1), pp. 138–149.

[10] Weiss, L. E., Merz, R., Prinz, F. B., Neplotnik, G., et al., 1997. "Shape deposition manufacturing of heterogeneous structures". *Journal of Manufacturing Systems,* ***16***(4), pp. 239–248.

[11] Stratasys. Polyjet process. `http://www.stratasys.com/polyjet-technology`. Accessed: 2018-03-08.

[12] 3DSystems. Multijet printer. `https://www.3dsystems.com/3d-printers/projet-mjp-2500-series`. Accessed: 2018-03-08.

[13] Arburg. Akf technique. `http://www.arburg.com/products-and-services/additive-manufacturing/akf-process/`. Accessed: 2018-03-08.

[14] Bruyas, A., Geiskopf, F., and Renaud, P., 2015. "Design and modeling of a large amplitude compliant revolute joint: The helical shape compliant joint". *ASME Journal of Mechanical Design,* ***137***(8), pp. 085003–085003–8.

[15] Bruyas, A., Geiskopf, F., and Renaud, P., 2015. "Toward unibody robotic structures with integrated functions using multimaterial additive manufacturing: Case study of an MRI-compatible interventional device". In IEEE/RSJ International Conference on Intelligent Robots and Systems, pp. 1744–1750.

[16] Evans, K., 1991. "Auxetic polymers: a new range of materials". *Endeavour,* ***15***(4), pp. 170–174.

[17] Mark, A. G., Palagi, S., Qiu, T., and Fischer, P., 2016. "Auxetic metamaterial simplifies soft robot design". In IEEE International Conference on Robotics and Automation, pp. 4951–4956.

[18] Maurin, B., Barbe, L., Bayle, B., Zanne, P., Gangloff, J., de Mathelin, M., Gangi, A., Soler, L., and Forgione, A., 2004. "In vivo study of forces during needle insertions". In Proceedings of 2004 Medical Robotics, Navigation and Visualization, pp. 415–422.

[19] Wang, Y., and Lee, K., 2017. "3D-printed semi-soft mechanisms inspired by origami twisted tower". In 2017 NASA/ESA Conference on Adaptive Hardware and Systems, pp. 161–166.

[20] Corbin, N., Vappou, J., Rao, P., Wach, B., Barbé, L., Renaud, P., de Mathelin, M., and Breton, E., 2016. "In vivo monitoring of percutaneous thermal ablation by simultaneous MR elastography and thermometry". In 24th annual meeting of the International Society for Magnetic Resonance in Medicine.

[21] Karnessis, N., and Burriesci, G., 2013. "Uniaxial and buckling mechanical response of auxetic cellular tubes". *Smart Materials and Structures,* ***22***(8), p. 084008.

[22] Azimian, H., Francis, P., Looi, T., and Drake, J., 2014. "Structurally-redesigned concentric-tube manipulators with improved stability". In IEEE/RSJ International Conference on Intelligent Robots and Systems, pp. 2030–2035.

[23] Masters, I., and Evans, K., 1996. "Models for the elastic deformation of honeycombs". *Composite structures,* ***35***(4), pp. 403–422.

[24] Gibson, L. J., and Ashby, M. F., 1997. *Cellular solids: structure and properties*. Cambridge university press.

[25] Tondu, B., and Lopez, P., 2000. "Modeling and control of mckibben artificial muscle robot actuators". *IEEE Control Systems,* ***20***(2), pp. 15–38.

[26] Kerscher, T., Albiez, J., Zöllner, J., and Dillmann, R., 2006. "Evaluation of the dynamic model of fluidic muscles using quick-release". In IEEE/RAS-EMBS International Conference on Biomedical Robotics and Biomechatronics, pp. 637–642.

[27] Chou, C.-P., and Hannaford, B., 1996. "Measurement and modeling of mckibben pneumatic artificial muscles". *IEEE Transactions on Robotics and Automation,* ***12***(1), pp. 90–102.

[28] Engelmann, F., 2007. Technologien im Produktentwicklungsprozess mit fokus auf produkte der biomedizinischen technik. Habilitation thesis, Otto-von-Guericke-Universität Magdeburg.

[29] Chatelin, S., Bernal, M., Papadacci, C., Gennisson, J. L., Tanter, M., and Pernot, M., 2014. "Anisotropic polyvinyl alcohol hydrogel phantom for shear wave elastography in fibrous biological soft tissue". In 2014 IEEE International Ultrasonics Symposium, pp. 1857–1860.